Cross section and neutron angular distribution measurements of neutron scattering on natural iron

E. Pirovano,[1] R. Beyer,[2] M. Dietz,[2,3] A. R. Junghans,[2] S. E. Müller,[2] R. Nolte,[4] M. Nyman,[1]
A. J. M. Plompen,[1,*] M. Röder,[2,3] T. Szücs,[2] and M. P. Takacs[2]

[1]*European Commission, Joint Research Centre, B-2440 Geel, Belgium*
[2]*Helmholtz-Zentrum Dresden-Rossendorf, D-01328 Dresden, Germany*
[3]*Technische Universität Dresden, D-01062 Dresden, Germany*
[4]*Physikalisch-Technische Bundesanstalt, D-38116 Braunschweig, Germany*

New measurements of the neutron scattering double differential cross section of iron were carried out at the neutron time-of-flight facilities GELINA and nELBE. A neutron spectrometer consisting of an array of up to 32 liquid organic scintillators was employed, which was designed to measure the scattering differential cross section at eight scattering angles and to simultaneously determine the integral cross section via numerical quadrature. The separation of elastic from inelastic scattering was achieved by analyzing the time-of-flight-dependent light-output distributions to determine the scattered neutron energy. The method was validated by studying elastic scattering on carbon and it was proved to work well for the determination of the elastic cross section. Here, the possibility to extend it to inelastic scattering was investigated too. For these experiments a sample of natural iron was used and the results cover the incident neutron energy range from 2 to 6 MeV. Both the differential and the integral elastic cross sections were produced for ^{nat}Fe, while for inelastic scattering, partial angular distributions for scattering from the first excited level of ^{56}Fe could be determined.

I. INTRODUCTION

For most nuclear facilities and equipment iron is a major structural material, and accurate neutron data are indispensable for their design and reliable operation. In nuclear power reactors, for instance, steel is typically used for the pressure vessel, to contain and support the fuel elements, for building the core structures and internals, and in some designs for reflectors and moderators. In charged-particle accelerators, where neutrons are mostly produced when the beam collides on the accelerator components (e.g., the energy degrader) or the surrounding media, iron is used in the bending and focusing magnets, beam pipes, and vacuum flanges. In these and other facilities the neutron energy spectra, flux distributions, and reaction and dose rates are influenced by the interaction with iron. The neutron transport models on which development, operation, and radioprotection requirements are usually based are affected, at times substantially, by the accuracy of the iron cross section data.

The uncertainties on the current evaluated nuclear data libraries of iron do not meet yet the target requirements for the development of advanced reactor systems. In [1] and [2], they are indicated among the main contributors to the uncertainty of the most important integral parameters (multiplication factor, reactivity coefficients) of the Generation-IV reactors. This is particularly important for the sodium-cooled fast reactors, whose design foresees the use of stainless steel reflectors to reduce neutron leakage. Moreover, discrepancies have been found between evaluated and experimental cross section in the fast neutron energy range. In [3], the results of a spherical shell transmission experiment were reported for three energies between 6 and 11 MeV, which suggested that the inelastic cross section in the ENDF/B-VII library should be 21% to 35% lower. For these reasons, inelastic scattering on ^{56}Fe was included in the High Priority Request List (HPRL) of the OECD-NEA Data Bank for nuclear data measurements [4]. The uncertainties on elastic scattering should be consistently lowered too [1], and the neutron angular distributions are an item on the INDEN (International Nuclear Data Evaluation Network) high-priority list [5].

The number of experiments regarding the scattering angular distributions available in EXFOR [6] for energies higher than 1 MeV is limited. For elastic scattering, differential cross sections were measured with high resolution in energy only up to 3 MeV; above 3 MeV, angular distributions were measured only for a restricted number of energies (see Table I). For inelastic scattering (Table II), there are no high-resolution measurements for the differential cross section above 2 MeV. The scarcity of experimental data poses a problem because the iron cross section is characterized by large fluctuations, which are difficult to model. Below 5 MeV, the predictions based on the optical model do not reproduce the behavior of the total cross section [7,8], which implies that elastic scattering, which is the dominant mechanism, is not

---

*arjan.plompen@ec.europa.eu

TABLE I. From the EXFOR database, measurements of the reaction cross section ("CS") and of the differential cross section with respect to the angle ("DA") of neutron elastic scattering on ^{nat}Fe, covering the incident neutron energy from 2 to 6 MeV. For each experiment, referred to by the name of the first author and the year of publication, the incident neutron energy range and the number of points are indicated.

Reference		Energy (MeV)	Quantity (Points)	
Becker (1966)	[9]	3.2		DA (14)
Begum (1981)	[10]	2.9		DA (11)
Beyster (1956)	[11]	2.5–7		DA (30)
Bostrom (1959)	[12]	3.67–4.7	CS (3)	DA (36)
Cierjacks (1978)	[13]	0.4889–3.0625		DA (18399)
Cranberg (1956)	[14]	2.25–2.45	CS (2)	DA (25)
Galloway (1979)	[15]	2.9		DA (9)
Gilboy (1965)	[16]	0.98–3.99	CS (4)	
Hill (1956)	[17]	5		DA (6)
Hill (1958)	[18]	5		DA (13)
Holmqvist (1969)	[19]	2.96–8.5	CS (5)	DA (60)
Holmqvist (1970)	[20]	1.77–2.76	CS (5)	DA (72)
Holmqvist (1971)	[21]	5.96	CS (1)	DA (13)
Hopkins (1964)	[22]	2–5		DA (7)
Jacquot (1966)	[23]	0.45–2.28	CS (8)	DA (264)
Kinney (1970)	[24]	4.6–8.56	CS (10)	DA (168)
Kinney (1976)	[25]	0.5–2.5	CS (2001)	DA (16008)
Korzh (1977)	[26]	1.5–3		DA (36)
Landon (1958)	[27]	2.2	CS (1)	DA (14)
Machwe (1959)	[28]	3.66	CS (1)	DA (24)
Pasechnik (1958)	[29]	2.8		DA (7)
Poole (1953)	[30]	2.5		DA (1)
Popov (1957)	[31]	2.9	CS (1)	DA (6)
Salnikov (1957)	[32]	2.34		DA (5)
Smith (1980)	[33]	1.684–3.905		DA (490)
Smith (1996)	[34]	4.5–9.99		DA (506)
Tomita (1970)	[35]	2.038–2.152		DA (54)
Tsukada (1961)	[36]	3.44–4.61		DA (59)
Tsukada (1969)	[37]	1.37–3.26		DA (5)
Walt (1955)	[38]	4.1	CS (1)	DA (11)

TABLE II. From the EXFOR database, measurements of the partial cross section ("CSP") or the partial differential cross section with respect to the angle ("DAP") of neutron inelastic scattering on ^{56}Fe, with partial meaning that only scattering from the first excited state is considered. The measurements cover the incident neutron energy from 2 to 6 MeV. For each experiment, referred to by the name of the first author and the year of publication, the incident neutron energy range and the number of points are indicated.

Reference		Energy (MeV)	Quantity (Points)	
Almén-Ramström (1975)	[39]	2.02–4.5	CSP (11)	
Barrows (1968)	[40]	2.9	CSP (1)	
Beyer (2014)	[41]	0.847–9.562	CSP (30)	
Boschung (1971)	[42]	5.05–5.58	CSP (2)	DAP (19)
Cranberg (1956)	[14]	2.25–2.45		DAP (26)
Degtjarev (1967)	[43]	1.37–3.76	CSP (7)	
Gilboy (1965)	[16]	2.01–3.99	CSP (3)	
Hicks (2015)	[44]	1.5–4.7	CSP (30)	
Kinney (1968)	[45]	4.6–7.55	CSP (7)	DAP (85)
Korzh (1977)	[26]	1.5–3.0	CSP (4)	DAP (35)
Lebedev (1977)	[46]	4.7		
Negret (2013)	[47]	0.861–4.50	CSP (645)	
Nemilov (1982)	[48]	0.893–2.115	CSP (25)	
		4.13–5.0	CSP (7)	
Rodgers (1967)	[49]	2.33	CSP (1)	
Salama (1981)	[50]	2.02–3.96	CSP (6)	DAP (100)
Schweitzer (1978)	[51]	3.4	CSP (1)	DAP (12)
Tomita (1970)	[35]	2.038–2.152		DAP (54)
Tsukada (1969)	[37]	1.37–4.49		DAP (73)

appropriately represented either. New experimental data describing the elastic scattering distributions would therefore provide important guidance for improving the model and the overall description.

The objective of this work is to provide new high-resolution data for the scattering differential cross section of iron in the fast neutron energy range of interest for fission technologies (1 to 6 MeV). For this, two time-of-flight (t.o.f.) measurements were realized, taking advantage of a neutron spectrometer developed at the t.o.f. facility GELINA of the Joint Research Centre in Geel (JRC-Geel) [52]. The spectrometer, which consists of an array of 32 liquid organic scintillators, is designed to measure the elastic differential cross section at 8 scattering angles and to simultaneously deduce the angle-integrated cross section. The data-analysis procedure, based on the deconvolution of the scintillator t.o.f.-dependent light output spectra for the identification of different reaction channels, was validated with a measurement of the standard cross section of neutron elastic scattering on carbon [52]. Here

we apply the same method for elastic scattering on iron and, in addition, we investigate the possibility of determining the inelastic scattering angular distributions too.

Two separate experiments were completed. The first was carried out in 2015 at the nELBE facility (Helmholtz-Zentrum Dresden-Rossendorf, HZDR), where a reduced version of the scintillator array with 16 detectors was employed. The second, in 2016, was at GELINA with the full 32-detector setup. For the two measurements, different iron samples and different data acquisition (DAQ) systems were used. This intercomparison was organised as an additional verification for the neutron spectrometer, and in particular to test the newly developed digitizer-based DAQ system installed at GELINA.

Instead of an expensive enriched sample, natural iron was considered sufficient as the first test case for the new spectrometer. ^{nat}Fe includes four isotopes and contains 91.8% of ^{56}Fe (see Table III). For elastic scattering, the contribution of the single species could not be disentangled; for this reason

TABLE III. Properties of ^{nat}Fe. The isotopic composition is is from [53], the molar mass from [54].

Fe isotope	^{54}Fe	^{56}Fe	^{57}Fe	^{58}Fe
Atom %	5.8(1)	91.8(1)	2.12(3)	0.28(1)
Molar mass		55.845(2) g/mol		
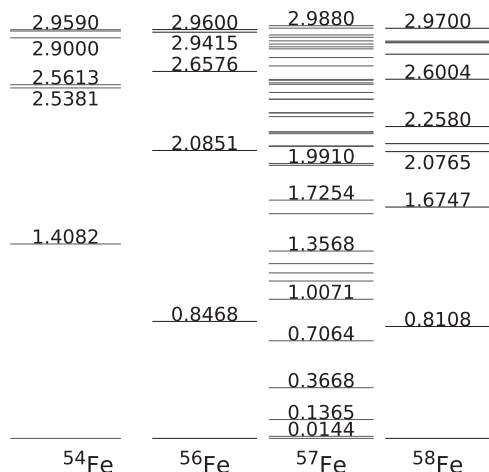
FIG. 1. Energy level structure of the iron isotopes. The energies (in MeV) of all excited states of ^{56}Fe up to 3 MeV [55] are indicated. For comparison, the first levels of ^{54}Fe [56], ^{57}Fe [57], and ^{58}Fe [58], and are indicated too.

the results are presented only for the natural mixture. For inelastic scattering it is possible in principle to discriminate between different nuclides by considering their level schemes (shown for ^{54}Fe, ^{56}Fe, and ^{57}Fe up to 3 MeV in Fig. 1). The energy resolution of the scintillators, however, does not allow one to distinguish between levels too close in energy, e.g., the level at 2941.5 keV and the following one at 2960.0 keV, and this restricts the results. We could establish that at least the first three excited states of ^{56}Fe can be distinguished reasonably well for scattering angles larger than 60° (laboratory frame of reference). At smaller angles, however, elastic scattering overshadows all other processes, and because of this only partial angular distributions could be determined. Here, only the results regarding the first excited level at 847 keV are presented. Given the low isotopic abundances and the scintillator energy resolution, it was not possible to account via data analysis for the contributions of ^{54}Fe, ^{57}Fe, and ^{58}Fe. Their impact is limited but nevertheless affects the final cross sections. The first four levels of ^{57}Fe from 14 to 706 keV, lying below the first of ^{56}Fe at 847 keV, and the first level of ^{58}Fe, all add to elastic scattering. Those higher than 847 keV but lower than the second level at 2085 keV (the first level of ^{54}Fe at 1408 keV and the ^{57}Fe levels from 1007 to 1991 keV) distort the determination of the inelastic scattering cross section of ^{56}Fe.

II. METHOD FOR THE DETERMINATION OF THE SCATTERING CROSS SECTIONS

The cross-section measurements described here are performed using a white neutron source to form a beam and irradiate a sample of the investigated material (the target). During the target irradiation, a neutron monitor is placed upstream to measure the incoming fluence, while an array of neutron detectors surrounds the target to count the scattered neutrons as a function of the angle. At the scattering angle θ, defined by the detector position relative to the neutron beam,

the differential cross section $\frac{d\sigma}{d\Omega}$ is then determined using the expression

$$\frac{d\sigma}{d\Omega}(E,\theta) = \frac{Y_{\mathrm{sc}}(E,\theta)}{\Delta\Omega\, N_n(E)\, n_T}, \tag{1}$$

where E is the incident neutron kinetic energy, Y_{sc} is the scattering reaction yield, $\Delta\Omega$ is the solid angle covered by the detector, N_n the number of incident neutrons on the target, and n_T the sample number areal density.

The detectors are placed at 8 different scattering angles, reported in Table IV, whose cosines correspond to the zeros of the Legendre polynomial of 8th order. This allows the use of the 8-point Gauss-Legendre quadrature to calculate the integral cross section σ, which can be expressed as

$$\sigma = 2\pi \int_{-1}^{1} \frac{d\sigma}{d\Omega}(\cos\theta)\, d(\cos\theta) \simeq 2\pi \sum_{i=1}^{8} w_i \frac{d\sigma}{d\Omega}(\cos\theta_i) \tag{2}$$

where θ_i are the angles, w_i the weight factors reported in Table IV, and $\frac{d\sigma}{d\Omega}(\cos\theta_i)$ is the differential cross section measured at θ_i. In general, the n-point Gauss-Legendre quadrature rule is constructed to give the exact result of $\int_{-1}^{1} p(x)\, dx$ for any polynomial $p(x)$ of order $2n-1$ or less.

Taking elastic scattering on ^{56}Fe as a reference, the evaluated nuclear data libraries (e.g., Refs. [59–61]) report coefficients up to the 7th order for energies below 3 MeV, and up to the 15th order below 6 MeV. Therefore, with 8 measurement points, it should be possible to completely characterise the angular distributions until 3 MeV. Above, the description is limited to the coefficients of highest order. The integration, however, should lead to an exact result over the whole energy range.

The kinetic energy E is obtained by applying the t.o.f. method: assuming that neutrons collide once in the target, their time of flight (from the source to the target and then to the detector) depends on the kinetic energy both before and after the collision (E and E', respectively), and can be written as

$$\mathrm{t.o.f.} = \frac{L}{c\sqrt{1 - 1/\left(1 + \frac{E}{mc^2}\right)^2}} + \frac{L'}{c\sqrt{1 - 1/\left(1 + \frac{E'}{mc^2}\right)^2}} \tag{3}$$

where c is the speed of light, m the neutron mass, and L and L' the lengths of the flight paths of the incident and scattered neutrons, respectively. It is possible to use this expression to determine E in the case of two-body reactions and provided that the interaction process (elastic scattering, inelastic scattering from the first excited state, etc.) is known. To apply Eq. (3), events where neutrons are detected must be separated from photons, the reaction channel must be identified, and multiple scattering events must be eliminated.

For scattering at a given angle θ, the relationship between E and E' can be derived from the energy conservation principle. In case of an elastic collision from a nucleus of mass M, E' is given, in the laboratory system, by

$$E'(Mc^2 + mc^2) - E(Mc^2 - mc^2) + E'E = c^2 p\, p' \cos\theta, \tag{4}$$

TABLE IV. Angles between the detector axis and the neutron beam direction, and corresponding weights for the application of the Gauss-Legendre quadrature rule. The 0.1° uncertainty represents the accuracy achieved in practice in the construction of the detector supporting structure.

Angle (deg)	163.8(1)	142.8(1)	121.7(1)	100.6(1)	79.4(1)	58.3(1)	37.2(1)	16.2(1)
Cosine	−0.9603(5)	−0.7967(11)	−0.5255(15)	−0.1834(17)	0.1834(17)	0.5255(15)	0.7967(11)	0.9603(5)
Weight	0.1012	0.2224	0.3137	0.3627	0.3627	0.3137	0.2224	0.1012

where $cp = \sqrt{E(E + 2mc^2)}$ and $cp' = \sqrt{E'(E' + 2mc^2)}$ are the neutron momenta before and after the collision. For inelastic scattering the equivalent expression is found by adding the excitation energy E^* of the target nucleus to its rest energy:

$$2E'(Mc^2 + mc^2) - 2E(Mc^2 - mc^2) + 2E'E$$
$$+ E^*(2Mc^2 + E^*) = 2c^2 p\, p' \cos\theta. \quad (5)$$

Solving Eq. (3) for the incident energy E requires knowing if the collision is elastic or inelastic. In practice, this problem was dealt with in the following manner: for each t.o.f. interval, a finite set of kinematically possible reactions was considered (elastic scattering always, inelastic scattering from applicable states) and the corresponding E was calculated ([e.g., for elastic scattering by combining Eqs. (3) and (4)]. Then depending on the measured value of the scattered neutron energy E', the appropriate reaction (and energy) was selected.

The identification of elastic and inelastic scattering reactions and the determination of the incident energy both rely on the measurement of the energy E'. For this reason, the neutron detectors used in the spectrometer are liquid organic scintillators. These are fast detectors with a time resolution of the order of 1 ns, sensitive to both fast neutrons and photons but allowing discrimination via pulse shape analysis, and therefore well suited for t.o.f. experiments. Moreover, they are are characterized by neutron spectrometry capabilities, so they can be used to measure the energy distribution of the scattered neutrons.

Neutron spectrometry with organic scintillators is possible after an accurate characterization of their response function; this can be achieved with a combination of calibration measurements and Monte Carlo simulations [62–65]. The detailed description of calibration measurements, simulations, and the validation of the whole procedure against a measurement of the standard neutron elastic cross section of carbon can be found in [52]. Here only the main points will be repeated. The photon response is determined by measuring the response to γ-emitter radionuclides, while for neutrons we carried out a t.o.f. experiment using carbon as scattering target. The simulations are implemented in the Monte Carlo n-particle transport code MCNP5 [66]. The geometry of the detector liquid cell and quartz optical window are replicated using the drawings provided by the manufacturer. To take into account possible backscattering, some details of the photomultiplier tube (namely the aluminium housing, mu-metal shielding and the glass vacuum envelope) are also included. The particle source consists of a monoenergetic beam of neutrons directly irradiating the detector. For each neutron crossing the sensitive volume, the deposited energy and the scintillation light output are calculated using the light output function parametrization

reported in [65] with coefficients derived from the calibration measurement with carbon. To deal with the nonlinearity of the scintillator light output function, and to properly handle the light produced when the neutron deposits its energy through multiple collisions (which is beyond the normal capabilities of MCNP), the MCNP "ptrac" output file has to be produced and post-processed. This produces the detector response matrix $R(L, E')$, defined as the probability for a neutron of energy E' to produce a light output signal of intensity L.

Neutrons characterized by an energy distribution $\Phi(E')$ produce a light output distribution $N(L)$ given by

$$N(L) = \int R(L, E')\, \Phi(E')\, dE'. \quad (6)$$

For a given scattering angle, the neutron energy distribution $\Phi(E')$ depends on the interaction of the beam with the target and in particular on which reaction channels are open at the given t.o.f. Assuming only scattering is possible, it can then be written as

$$\Phi(E') = \sum_{i=0}^{I_{max}} Y_{sc,i}\, \delta(E' - E_i), \quad (7)$$

where E_i is the neutron energy after scattering from the ith excited state, $Y_{sc,i}$ is the corresponding reaction yield, and the sum goes from the ground state ($i = 0$, elastic scattering) to the highest possible level allowed by the kinematics I_{max}. The resulting spectrum $N(L)$ is a sum of terms in the form of $\varepsilon_{geo} Y_{sc,i} R(L, E_i)$ (where ε_{geo} is the geometrical efficiency), which means that the reaction yields can be simply determined from a linear fit.

The limit of this method is that the reaction identification can only happen at the level of distributions and not event by event, and the determination of the yields is heavily influenced by the accuracy of $R(L, E')$. In [52], it was proved that the numerical technique used for the modeling (the MCNP ptrac file post-processing) produces reliable results to the extent that the data used to describe the detection process are accurate. In organic scintillators the predominant neutron interaction in the energy range we are aiming at is elastic scattering on hydrogen nuclei. The shape of $N(L)$ mainly reflects the angular distribution of n-p (if the natural hydrogen isotopic composition is used) or n-d (for deuterated solutions) scattering. For this reason we decided to have both deuterated and nondeuterated detectors in the spectrometer, as the different responses give a means to check for self-consistency during the data analysis.

In the proof-of-principle measurement, the experimental differential and angle-integrated cross sections of carbon were determined with uncertainties ranging from 9% to 15% on the angular data and from 5% to 10% on the integral. The results

were found to be compatible with the evaluation from the ENDF/B-VII.1 library in the energy range from 2 to 8 MeV, within one standard deviation for the integral. Above 8 MeV, the low incident fluence limited the statistics and, accordingly, the precision. Below 2 MeV, the analysis produced inaccurate results because the neutron energy was too close to the detection threshold, which was set to a somewhat high value to avoid spurious events and improve the neutron/photon discrimination, and because the detector response functions could not be verified in detail owing to the impact of multiple scattering at low amplitudes.

III. FACILITIES AND EXPERIMENTAL CONDITIONS

Both GELINA [67,68] and nELBE [69] are electron-linac accelerator-driven sources in which bremsstrahlung photons and neutrons from photonuclear reactions are produced when electron pulses of short duration (less than 1 ns for GELINA, 5 ps for nELBE) impinge on a high-atomic-number target (depleted uranium at GELINA, liquid lead at nELBE). The white-spectrum neutrons, covering energies up to 10 MeV (nELBE) and 20 MeV (GELINA), are first collimated to form a beam, then directed on the scattering target.

At GELINA the experimental setup was installed along the flight path at $108°$ from the electron beam, in the measurement cabin placed at the nominal distance of 30 m from the neutron source. The neutron beam travels from the target hall to the measurement cabin in a tube of 50 cm diameter kept under vacuum. Along the tube, collimators made of copper (fast neutron absorber), lithium epoxy (for slow neutrons), and lead (photons) are installed to define the beam size. Two filters, 2 cm of depleted uranium and 1 cm of boron carbide, are used to reduce the intensity of bremsstrahlung and thermal neutrons, respectively. The beam profile was measured with a photographic film and a neutron camera, obtaining a beam diameter of 4.6(1) cm at the exit of the tube and 4.9(2) cm at the scattering target position.

At nELBE, the beam is collimated by a steel tube with lead and borated polyethylene inserts placed at $100°$ with respect to the primary electron beam. To reduce the photon fluence on the target, a lead absorber of 3 cm thickness was set up in front of the neutron beam collimator. The experimental hall is separated from the neutron radiator by a 2.5 m thick wall of heavy concrete. There, the detector setup was located at 8.3 m from the neutron radiator. The beam diameter at the target position of 7.39(2) cm was deduced in this case from the results of previous measurements [69].

In both experiments, a 3-mm-thick disk of natural iron was employed as neutron target (see Table V). For the experiment at GELINA, the disk was placed at 27.037(5) m from the neutron source, while at nELBE the neutron flight path was 8.300(5) m long. The fission chamber was positioned upstream the iron target, at 1.37 m distance at GELINA and 2.256 m at nELBE. The measurements with the iron sample ("sample-in") were accompanied with "sample-out" measurements, during which data were collected with the empty frame, after removing the scattering sample, to establish the background. The irradiation time for the sample-in and sample-out runs and the other quantities describing the

TABLE V. Dimensions and areal densities (measured quantities) of the two iron samples used at the two facilities, GELINA and nELBE.

	Thickness (cm)	Diameter (cm)	Mass (g)	Areal density (g/cm^2)
GELINA	0.30(1)	7.103(1)	96.215(5)	2.4283(7)
nELBE	0.31(1)	7.90(1)	119.689(1)	2.442(6)

experimental conditions are also summarized in Table VI. The t.o.f. resolution corresponds to the full width at half maximum (FWHM) of the distribution of the arrival time of the bremsstrahlung photons, the so-called γ flash. The resolution of 5 ns at GELINA and 1 ns at nELBE translates for 1 MeV neutrons to an energy resolution of 5 keV and 3 keV respectively.

IV. NEUTRON SPECTROMETER AND DATA ACQUISITION

The neutron spectrometer is shown in Fig. 2. It includes a ^{235}U fission chamber for the measurement of the incoming neutron flux and 32 liquid organic scintillators for the detection of the scattered neutrons.

The scintillators are arranged in four sets of eight; for each set, the detectors are mounted at the angles specified in Table IV, where the uncertainty of $0.1°$ corresponds to the accuracy achieved in the construction of the supporting frame. The distance between their front faces and the center of the target is 30.0(3) cm. The detectors are commercially available liquid organic scintillators manufactured by Scionix: two sets of eight are filled with the EJ301 scintillation liquid [70] (NE213 equivalent; detector model 51A51/2MQOE1-EJ301-NX), the other two sets with EJ315 [71] (C_6D_6 equivalent; model 51A51/2MQOE1-EJ315-NX). Both have cylindrical liquid cells with 5.08 cm diameter and 5.08 cm height.

The fission chamber is a parallel-plate ionization chamber containing eight UF_4 deposits enriched to 99.94% with ^{235}U, arranged on three double-sided and two single-sided aluminium foils, for a total ^{235}U areal density of 4.095(4) mg/cm^2.

TABLE VI. Comparison of the experimental conditions at GELINA and nELBE. (FC = fission chamber).

		GELINA	nELBE
Flight path	source-FC (m)	25.667(5)	6.044(5)
	source-target (m)	27.037(5)	8.300(5)
	target-detector (m)	0.300(3)	0.300(3)
Beam time	sample-in (h)	123.8	78.4
	sample-out (h)	71.2	20.3
Avg. flux on target [10^4 n/(cm^{2}s)]		2.965(2)	1.076(2)
LINAC repetition rate (Hz)		800	101×10^3
T.o.f. resolution (ns)		5	1
Energy resolution at 1 MeV (keV)		5	3
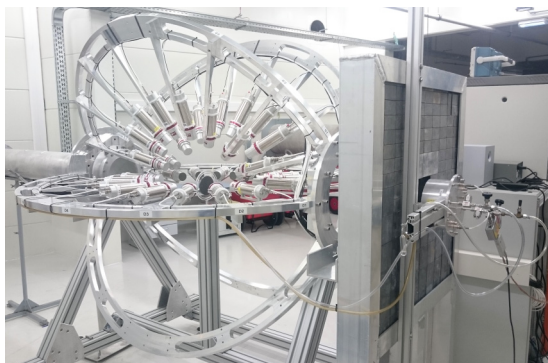
FIG. 2. Picture of the setup installed in the measurement station at 108°, 30 m distance from the GELINA neutron source. The neutron beam comes from the right; it first passes through the fission chamber, then hits the target at the center of the scintillator array. The fission chamber is mounted on a lead wall which is the last beam collimator.

For the measurements at GELINA, a dedicated digitizer-based acquisition system was developed to collect the anode signals produced by the 32 scintillators. It consists of eight digitizer cards with four input channels each, 14 bit resolution, and 500 MS/s sampling rate (SP Devices, model ADQ14DC-4A-VG-PXIe). To synchronize the digitizer clocks an external 10 MHz reference is provided by a clock generator (Stanford Research Systems Inc. CG635). Every waveform produced by the scintillators and the respective timestamps are saved to disk for offline processing. The processing includes the determination of the total integrated charge (proportional to the light output produced in the event), the correction of the timestamp, and the pulse shape analysis. The correction of the timestamp (a leading-edge trigger) is to improve the time resolution; this is achieved by analyzing the waveforms applying the constant fraction discriminator (CFD) algorithm [72,73]. For the pulse shape analysis, the charge integration method [74] is applied, according to which the pulse shape discrimination (PSD) factor is defined as the ratio between the integral of the tail to the total integral of the signal waveform.

The DAQ system of the fission chamber consists of conventional front-end electronics. The fission chamber output is first fed to a charge-integrating preamplifier (CSTA2HV from the Technische Universität Darmstadt), and then it is split in two. It is given to a spectroscopy amplifier (Ortec 671) and to an analog-to-digital converter (ADC, FAST ComTec 7072), and, in parallel, to a fast filter amplifier (Ortec 579), a constant fraction discriminator (CFD, Ortec 584) and a time-to-digital converter (TDC, JRC in-house development). A multiplexer (MMPM, JRC in-house development) controls the ADC and TDC, ensuring the coincidence between amplitude and time information, and redirects the data to the PC where they are stored in the form of list files.

The data acquisition system at nELBE [69] is based on commercially available VME modules including ADCs (CAEN 1785N), QDCs (charge-to-digital converters, CAEN V965), CFDs (HZDR in-house development), and TDCs (CAEN V1290A). The DAQ dead time due to the analog-to-digital conversion is measured per event and a t.o.f.-dependent

dead time correction is applied using the procedure described in [69]. For the scattering experiments, the scintillator signals were split and fed to two QDC channels for the charge integration over a long and a short interval, and to a CFD channel which was in turn connected to a TDC and the trigger logic module. The TDC gathered the signals from both the detectors and the accelerator reference signal, determining in this way the time of flight. For the fission chamber, the signal-processing chain was identical to that used at GELINA.

V. DATA ANALYSIS

The neutron fluence incident on the iron target is determined utilizing the standard ^{235}U(n, f) cross section to correlate the fission fragment counts in the chamber with the number of incident neutrons. The data-analysis procedure has been already outlined in several other papers reporting measurement with fast neutrons at GELINA. For instance, it can be found in [75].

The analysis of the scintillator data aims at the determination of the scattering reaction yields; but before that, the photon and neutron events are separated, the background is subtracted, and multiple scattering events are removed. First, the detected photon-induced events are separated from the neutron-induced events, and this is accomplished through the pulse shape analysis of the anode signals of the scintillators. Several algorithms are available but they do not differ much in terms of performance [76], therefore we opted for the well-established and simple-to-implement charge integration method [74,77]. After the separation, the resulting neutron time-of-flight distributions (see Fig. 3 for example) are corrected for the background. Two main components have been identified: the time-independent room-return neutrons and the time-dependent background due to beam neutrons scattering in air in the path between the end of the flight-path tube and the scattering target. The average room-return contribution per t.o.f. channel can be assessed by averaging the counts at long t.o.f. values falling between the neutron bursts (for example after 5000 ns at GELINA and 1300 ns at nELBE). The subtraction does not affect much the t.o.f. distributions of GELINA [see Figs. 3(a) and 3(b)], while for nELBE the correction is substantially higher [Figs. 3(c) and 3(d)]. This is because the accelerators have very different repetition rates (800 Hz for GELINA and 101 Hz for ELBE); even if the random background counting rate is comparable at the two facilities, the contributions per t.o.f. bin differ by about two order of magnitude. The time-dependent background is first determined during the sample-out run, then subtracted from the sample-in measurement after normalization with the monitor counts (fission fragment counts summed over the whole t.o.f. range). This background component has been found to give rise up to 30% of the counts per t.o.f. channel, therefore the statistics collected during the sample-out run impacts the precision of the final results. We later realized that the sample-out run at nELBE (1/4 of the total measurement time) was too short: this can be seen for example in the large relative errors in measured light-output distributions shown in Fig. 5 (explained later on). For this reason, for the
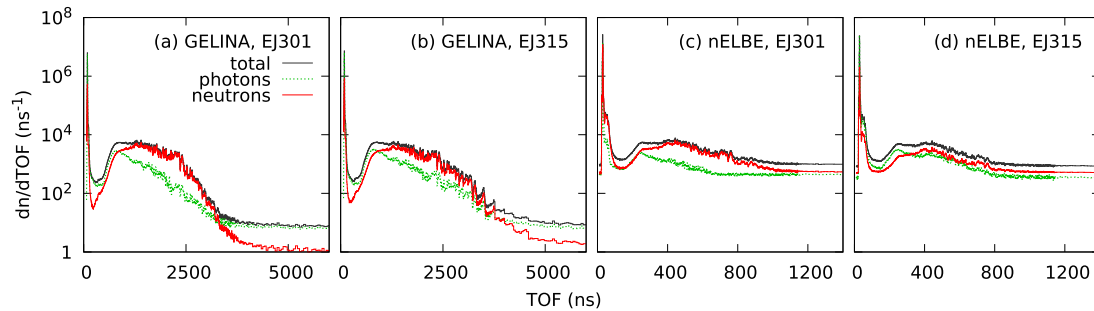
FIG. 3. T.o.f. distributions measured at GELINA [(a) and (b)] and nELBE [(c) and (d)] with an EJ301 detector [(a) and (c)] and an EJ315 detector [(b) and (d)] at 100.6° (same detector at the same position at both facilities), different irradiation times (see Table VI).

second experiment at GELINA we took nearly equal times for sample-in and sample-out runs.

In case of multiple-scattering events in the iron disk, the time-energy relationship cannot be defined in simple terms, so the straightforward solution to determine their contribution is to deduct it from the data analysis. This is achieved with an MCNP simulation reproducing the detector array configuration and using the measured beam diameter and energy distribution to define the neutron source. Of all neutrons reaching any given scintillator, the fraction of those arising from multiple-scattering events is tallied, determining in this way a time-of-flight-dependent and detector-dependent correction factor eliminating multiple scattering events.

Having eliminated photons, background, and multiple scattering events, it is finally possible to proceed with spectrometry for the identification of scattering reactions. The data are sorted in t.o.f. intervals corresponding to the effective

t.o.f. resolution (5 ns at GELINA, 1 ns at nELBE), and for each interval the corresponding light output spectrum is built up. Then, interval by interval, the theoretical distribution $Y_{el} R(L, E_{el}) + \sum_{i=1}^{3} Y_{in,i} R(L, E_{in,i})$ obtained for the sum of the contribution of elastic scattering (el) and inelastic scattering from the first three excited states (in$_1$, in$_2$, and in$_3$ for the levels at 847, 2085 and 2658 keV respectively) is fitted to the data to determine the reaction yields Y. The differential and angle-integrated cross sections then follow from Eq. (1) and the quadrature in Eq. (2).

In Figs. 4 and 5, the light-output spectra measured at different angles for the t.o.f. interval corresponding to 3.31–3.34 MeV incident energy on the target are presented. The measurements are compared with the result of the fit of the simulated spectra to the data. In these two figures it is possible to notice the difference between EJ301 and EJ315 detectors. Being deuterated detectors (with a nominal ^{1}H to
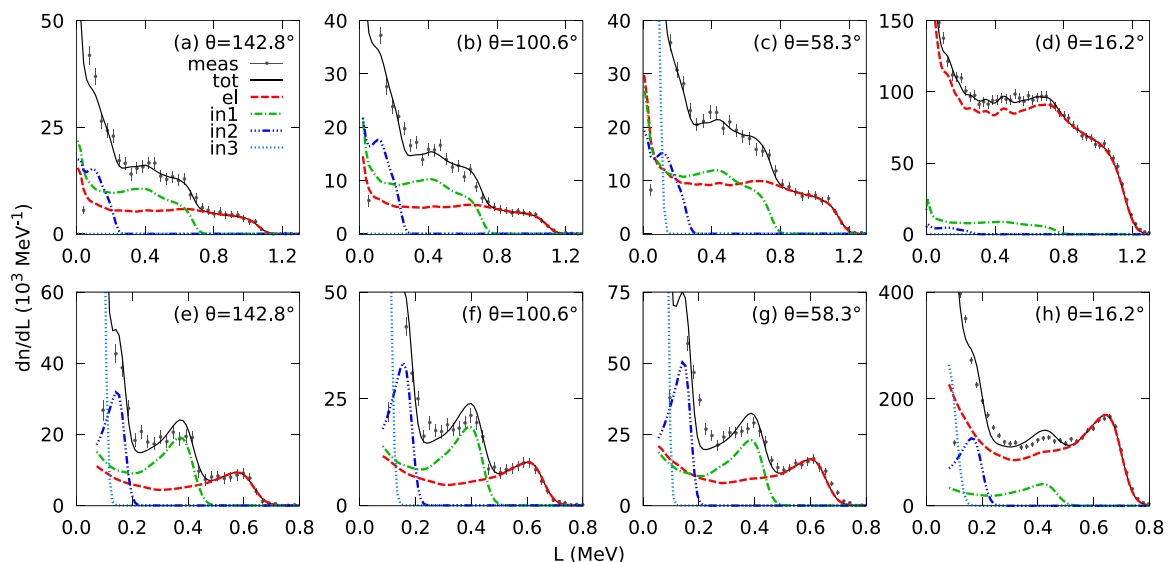
FIG. 4. Light output distributions (in equivalent electron energy deposition) for EJ301 [(a) to (d)] and EJ315 detectors [(e) to (f)] at different angles θ. The measurements were carried out at GELINA, and correspond to the t.o.f. interval from 1086 to 1091 ns. If elastic scattering is considered, it corresponds to an incident neutron energy of 3.31–3.34 MeV. This value represents a lower limit: for any other nonelastic reaction, the same t.o.f. interval corresponds to higher energies. The measurements (meas) are compared with the detector response modeled for elastically scattered neutrons (el), for inelastic scattering from the first three levels of ^{56}Fe (in$_1$, in$_2$, and in$_3$ for the levels at 847, 2085, and 2658 keV respectively), and their sum (tot = el + $\sum_{i=1}^{3}$ in$_i$).
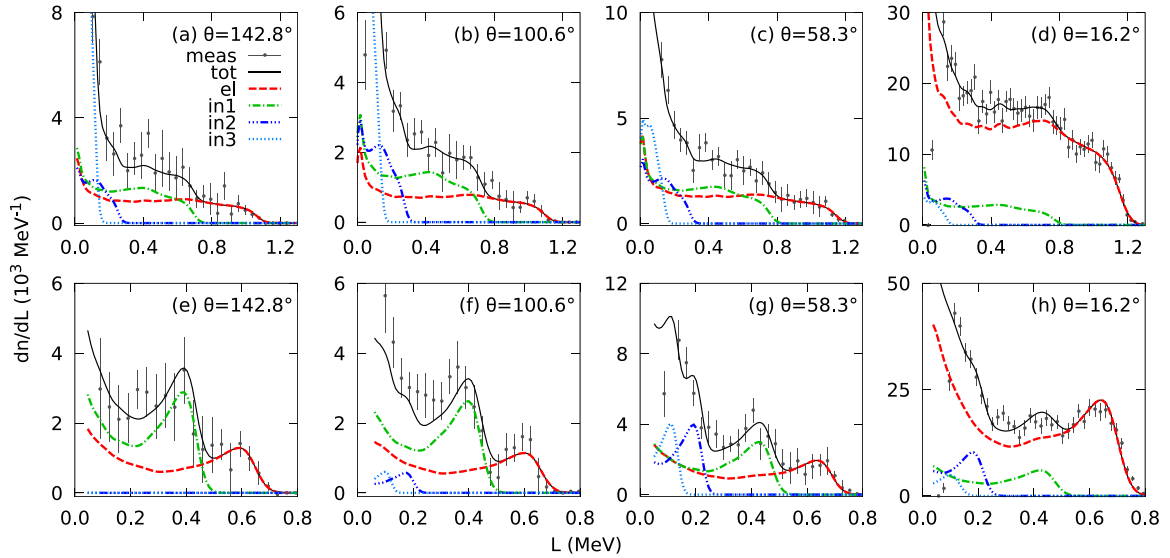
FIG. 5. Same as for Fig. 4 but for measurements at nELBE, for the t.o.f. interval from 343 to 344 ns, corresponding to an incident neutron energy for elastic scattering of 3.31–3.33 MeV. Panels (a) to (d) refer to EJ301 and panels (e) and (f) to EJ315 detectors.

^{2}H ratio of 1 to 141), the EJ315 response mainly reflects the backward-to-forward asymmetry of *n*-*d* scattering. This feature makes it simpler to identify the monoenergetic groups forming the energy distribution. However, the model of the detector response is somewhat less reliable as there are some documented issues with the *n*-*d* evaluated differential cross section [78,79]. The discrepancies [e.g., in Fig. 4(e) or 4(f) at 0.35–0.4 MeV] between measured and simulated spectra might be due to the library used in MCNP (ENDF/B-VII.1 in this case). The modeling of the EJ301 detectors is much

more reliable as it is based on the standard *n*-*p* cross section [80]; however, the analysis is more complicated because of the relatively flat distribution.

Overall, the light-output distributions are well reproduced by the simulations. There are not always sufficient points to fit the yield of the third level [see Figs. 4(a), 4(b), 4(d), 5(e)]; however, with the first two excited levels and elastic scattering it is possible to reproduce the measured spectra above 100 keV (light output in equivalent electron energy deposition). As elastic scattering is mostly forward peaked
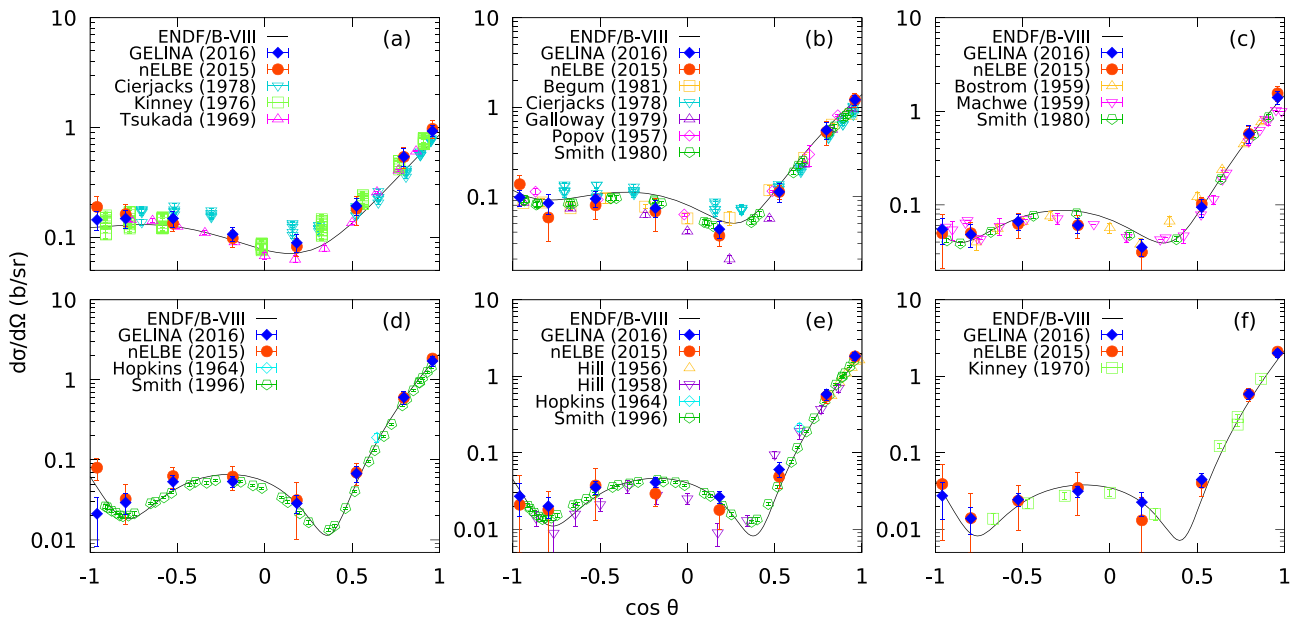
FIG. 6. Differential cross section $\frac{d\sigma}{d\Omega}$ of elastic scattering on ^{nat}Fe as a function of the cosine of the scattering angle in the laboratory system θ, for selected intervals of incident neutron energy E: (a) $E = 2.002$–2.016 MeV, (b) $E = 2.894$–2.919 MeV, (c) $E = 3.635$–3.671 MeV, (d) $E = 4.455$–4.503 MeV, (e) $E = 4.973$–5.030 MeV, (f) $E = 5.521$–5.587 MeV. The results of the measurements at GELINA and nELBE are compared with other experiments and the angular distribution reported in the ENDF/B-VIII library.
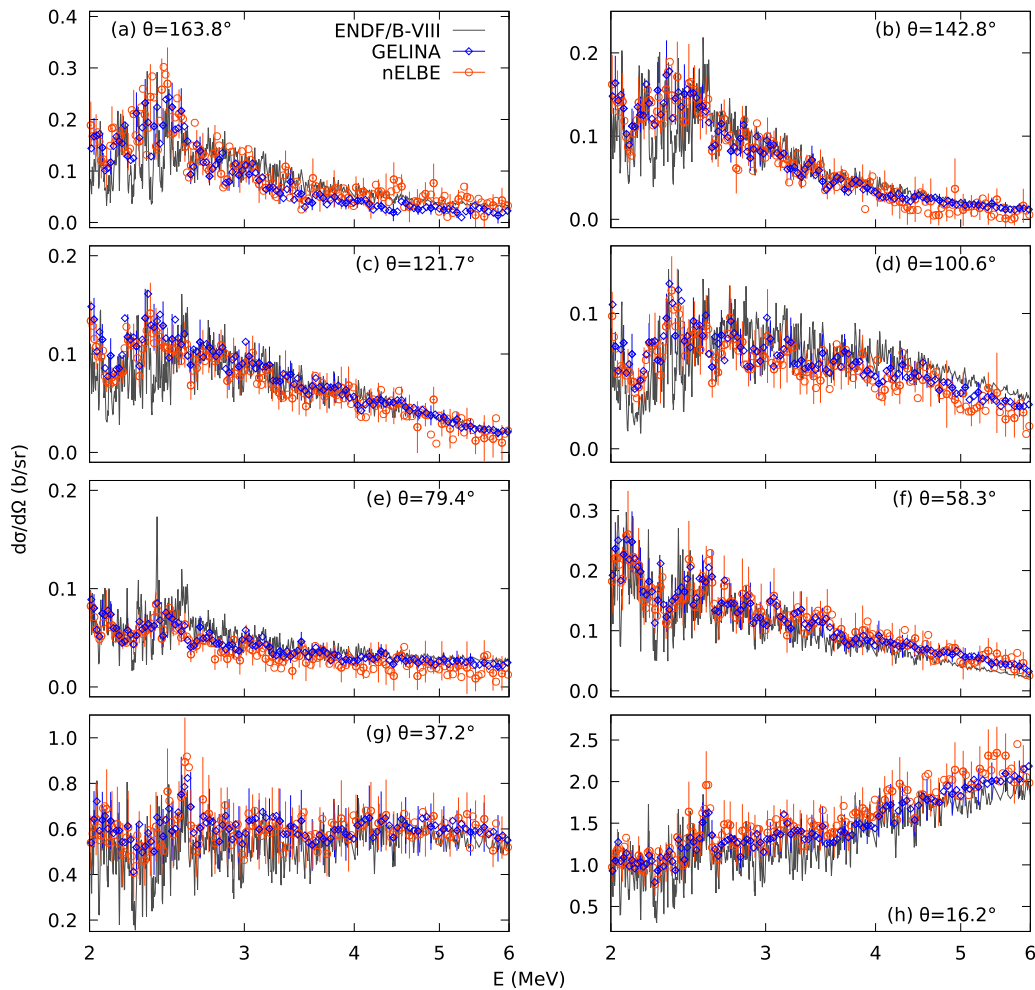
FIG. 7. Differential cross section $\frac{d\sigma}{d\Omega}$ of elastic scattering on ^{nat}Fe as a function of the neutron incident energy E: comparison of the measured values with the ENDF/B-VIII evaluation at the laboratory angles θ. To improve the readability of the graphs, the experimental uncertainties are given every third point.

while inelastic scattering is almost isotropic and the cross sections have one order of magnitude difference, at forward angles the elastic reactions give rise to most of the counts. At this energy the separation of inelastic scattering is less precise but still possible. At higher energies the fitting procedure does not give reliable results anymore, and for the three most forward angles separation is not possible.

VI. ELASTIC SCATTERING CROSS SECTION

The elastic scattering cross section results are shown in Figs. 6, 7, and 8. In Fig. 6 the differential cross section is presented as a function of the scattering angle cosine for six different energy bins, chosen to compare the two experiments at GELINA and nELBE with the already existing measurements (from the EXFOR database, see Table I for references) and the ENDF/B-VIII evaluation. In Fig. 7, the cross section is presented by angle, as a function of the energy. The angle integrated cross section is shown in Fig. 8. Also in this case, our data are compared with other measurements [Fig. 8(a)] and the ENDF/B-VIII evaluation averaged according to the experimental energy resolution [Figs. 8(b) and 8(c)]. The

cross section is presented in the incident neutron energy range from 2 to 6 MeV: the carbon experiment proved that the results below 2 MeV are unreliable, and above 6 MeV the statistical fluctuations are such that the relative uncertainties amount to almost 50%.

The GELINA and nELBE datasets are compatible with each other over the whole energy range [see for instance the direct comparison in Figs. 7 and 8(a)]. They are so close to each other that it is reasonable to conclude that the new DAQ development is validated.

The total uncertainties on the differential cross section range from 20% to 40% for the measurements at GELINA and from 20% to 50% for nELBE, and they are mostly due to statistics (of both the sample-in and sample-out runs). In both cases the highest uncertainties are found at backward angles for energies above 5 MeV, where the count rate is low because of the physics of the process. Elastic scattering on iron is a strongly forward-peaked reaction: there is almost one order of magnitude difference between the differential cross section at the most forward angle (16.2°) and the angles larger than 60° (79.4°, 100.6°, 121.7°, 142.8°, and 163.8°). The only way to reduce the uncertainties at
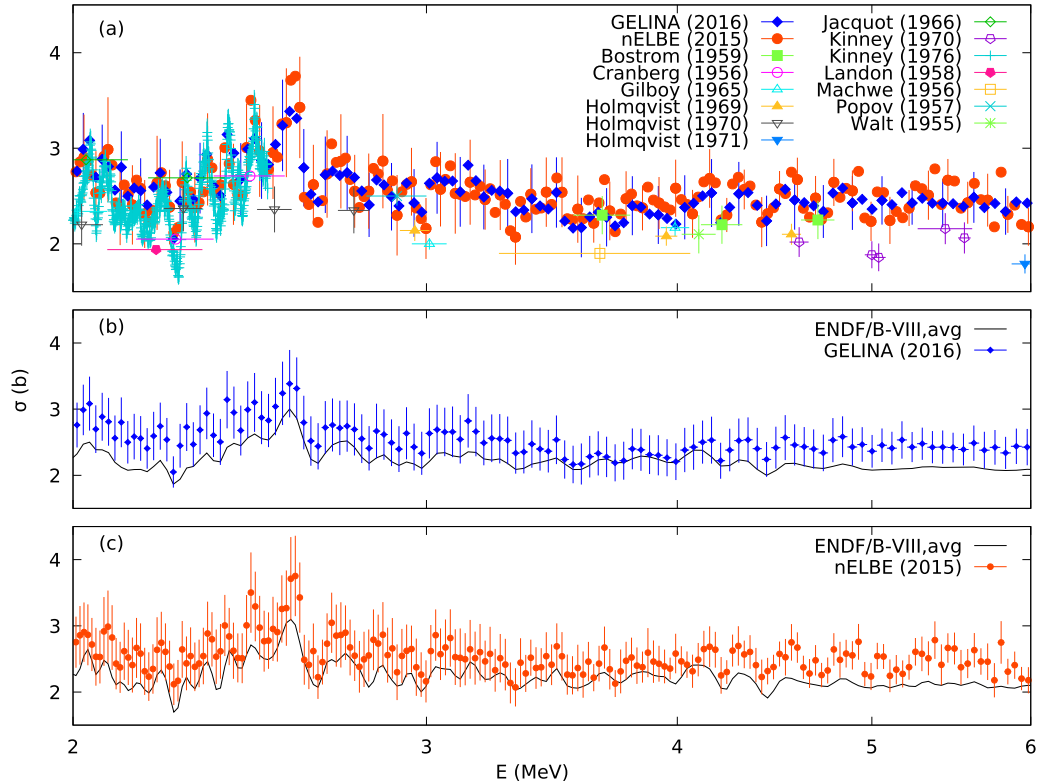
FIG. 8. Angle-integrated cross section σ of elastic scattering on ^{nat}Fe as a function of the incident neutron energy E: comparison with previous measurements (a), and with the ENDF/B-VIII evaluation averaged ("ENDF/B-VIII,avg") according to the experimental energy resolution (b,c).

those angles would be to make longer measurements. For the angle-integrated cross sections, the uncertainties vary between 10% and 14% for GELINA, and between 10% and 18% for nELBE.

The agreement with the other existing experimental results is overall good. The uncertainties are in general higher in our data than in the other measurements, but on the other hand we cover an energy range where there are only a few data points
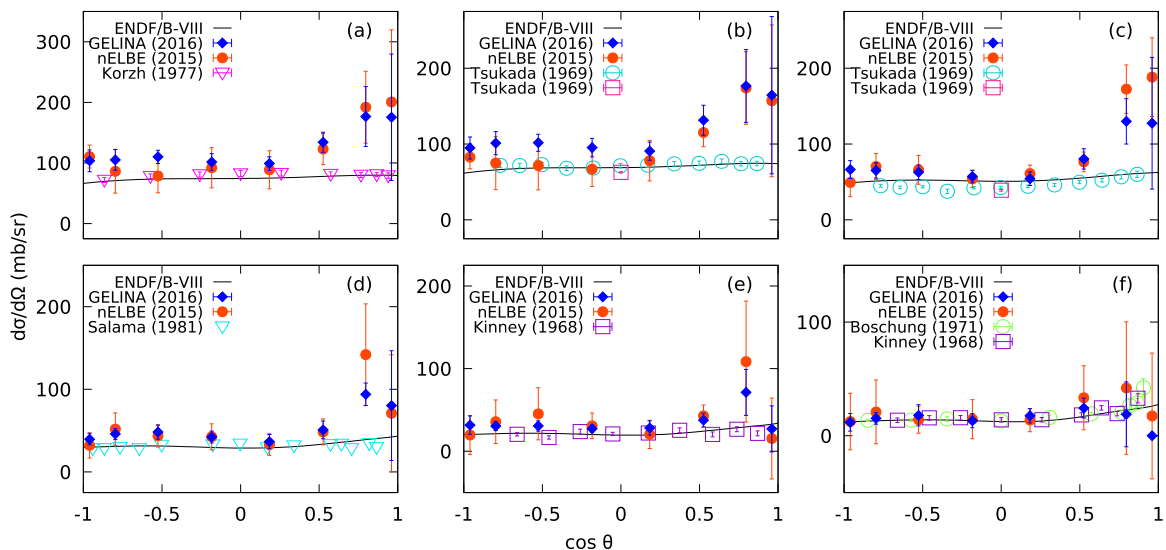
FIG. 9. Differential cross section $\frac{d\sigma}{d\Omega}$ of inelastic scattering from the first level of ^{56}Fe as a function of the cosine of the scattering angle in the laboratory system θ_{LAB}, for selected intervals of incident neutron energy E: (a) $E = 2.493–2.513$ MeV, (b) $E = 2.638–2.660$ MeV, (c) $E = 3.248–3.278$ MeV, (d) $E = 3.934–3.973$ MeV, (e) $E = 4.552–4.601$ MeV, (f) $E = 5.521–5.587$ MeV. The results of the measurements at GELINA and nELBE are compared with other experiments and the angular distribution reported in the ENDF/B-VIII library.
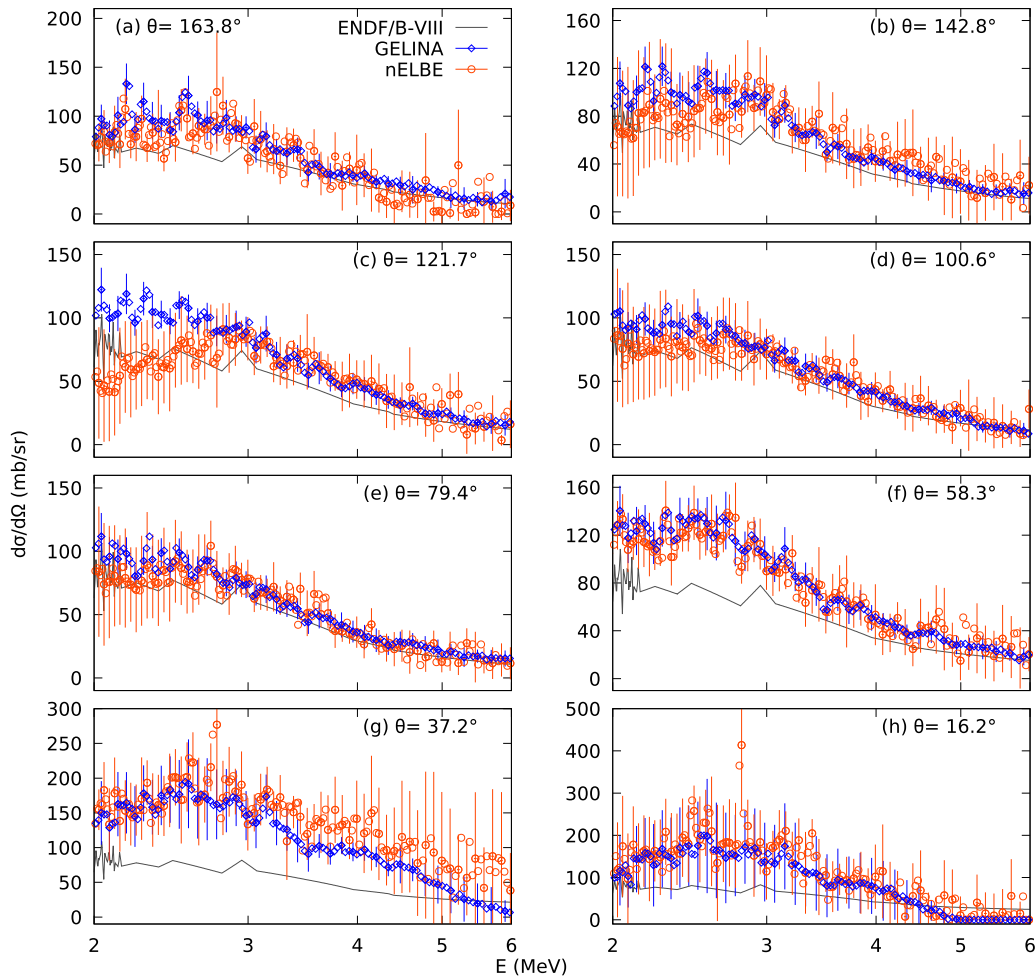
FIG. 10. Differential cross section $\frac{d\sigma}{d\Omega}$ of inelastic scattering from the first level of ^{56}Fe as a function of the neutron incident energy E: comparison of the measured values with the ENDF/B-VIII evaluation at the laboratory angles θ. To improve the readability of the graphs, the experimental uncertainties are given every third point.

(see Table I) and, compared to most cases, they have a better energy resolution.

Both GELINA and nELBE datasets are compatible with the ENDF/B-VIII nuclear data library [Figs. 8(b) and 8(c)], chosen for this comparison as it includes the latest results of the CIELO evaluation [59]. The compatibility is good between 3 and 4 MeV. In the rest of the energy range the measurements are systematically higher than the evaluation, with the discrepancy comparable to the uncertainty band. Regarding the differential cross sections, this effect can be observed mostly in the forward direction, at 58.3° [Fig. 7(f)] and to a lesser extent at 16.2° [Fig. 7(h)].

In the evaluation the elastic cross section is defined as the difference between the total and the remaining partial cross sections [81]; the systematic difference between experiment and evaluation therefore might be an effect of this procedure. The evaluators indeed already noticed a slight underestimation of the Kinney data [45]. This goes in the same direction as the conclusions of [3], where it is suggested that the ENDF elastic cross section should be higher. There the discrepancy is found to be 21% at 6 MeV; however, here it is not higher than 13%.

VII. INELASTIC SCATTERING CROSS SECTION

The differential cross section of neutron inelastic scattering from the first excited level of ^{56}Fe is shown in Figs. 9 and 10. Similarly as for elastic scattering, it is first presented as a function of the scattering angle cosine for six different energy intervals in Fig. 9. In Fig. 10, the results are presented by angle, as a function of the incident neutron energy.

The GELINA and nELBE cross sections are overall compatible with each other. At 121.7°, however, below 3 MeV, the differential cross section measured at nELBE decreases with the neutron energy, while the cross section measured at GELINA remains more or less constant. As the only difference between the two measurements is the data taking process, the reason for this discordance has to be sought in the raw data rather than in the analysis procedure. However, no sign of detector malfunctioning was found; on the contrary, the calibration measurements showed a very stable detector response. We could find no reason that would allow us to correct or justify the rejection of the data.

In general, the measurements at GELINA are affected by uncertainties that in most cases range from 20% to 50%,

while for the nELBE data the uncertainties vary between 20% and 60%. This becomes particularly problematic for the two most forward detectors, for energies above 4 MeV. This is because inelastic scattering is determined after the subtraction of the elastic scattering contribution. At forward angles, while the inelastic cross section decreases with the neutron energy, the elastic cross section keeps increasing. The predominance of elastic scattering becomes critical, for example, at $16.2°$ above 5 MeV: for this energy, the elastic cross section is two orders of magnitude higher than that of inelastic scattering. With the current statistics, the inelastic scattering events become indistinguishable; for this reason, in Fig. 10(h), the experimental differential cross section above 5 MeV goes to zero. For the second-most forward angle ($37.2°$), the problem is similar: above 4 MeV, the uncertainties range from 40% to 100%. When comparing with previous measurements, one finds that the cross section at $16.2°$ and $37.2°$, and also partially at $58.3°$ [Figs. 10(f) to 10(h)], is largely overestimated. This affects the angle-integrated cross section so severely that we have chosen not to present it here.

All this indicates that for the accurate determination of the inelastic scattering cross section higher statistics or a more sophisticated procedure for the separation of the various scattering components, such as proper unfolding of the scintillators light output distributions, are necessary.

VIII. CONCLUSIONS

New measurements of the double differential cross section of neutron elastic scattering on iron have been carried out at the time-of-flight facilities GELINA and nELBE. A neutron spectrometer consisting of an array of 32 scintillators was employed to cover the incident neutron energy range from 2 to 6 MeV. It is possible to separate elastic and inelastic scattering using a method based on the determination the neutron energy before and after the collision. The method is based on the analysis of the t.o.f.-dependent light output spectra, and relies on a combination of calibration measurements and MCNP Monte Carlo simulations for the accurate determination of the scintillator response function.

The scattering target was a sample of natural iron. The energy resolution of the scintillators does not allow the discrimination among isotopes for elastic scattering, therefore the results can refer to the natural isotopic composition only. The data were corrected for room return and in-air scattering by alternating sample-in and sample-out measurements. For the multiple scattering correction, an MCNP simulation was implemented replicating the setup and using the measured neutron energy distribution. The differential elastic cross section was determined at eight angles and the integral cross section was deduced applying the Gauss-Legendre quadrature technique. The results agree overall well with previous measurements, but they are systematically higher than the ENDF/B-VIII evaluation.

The uncertainties on the differential cross section range from 20% to 40% for the measurements at GELINA and from 20% to 50% for nELBE. For the angle-integrated cross sections, the uncertainties vary between 10% and 14% for GELINA, and between 10% and 18% for nELBE. The uncertainties do not necessarily meet the requirements (it is difficult to say as for elastic scattering the requirements are not explicitly stated in the HPRL); however, the results cover an energy range where barely any measurement is available. Moreover, having proved the feasibility of this type of measurement, it will be possible in the future to organize more extended measurement campaigns with, e.g., enriched iron samples.

An attempt to investigate inelastic scattering from the first level of ^{56}Fe was made; however, the separation from the elastic scattering turned out to be quite problematic, in particular at forward scattering angles (because of the different orders of magnitude in the elastic and inelastic cross sections). Therefore, only partial angular distributions could be produced, with uncertainties that range from 20% to 50% at GELINA, and from 20% to 60% at nELBE.

[1] G. Aliberti, G. Palmiotti, M. Salvatores, T. Kim, T. Taiwo, M. Anitescu, I. Kodeli, E. Sartori, J. Bosq, and J. Tommasi, Ann. Nucl. Energy **33**, 700 (2006).

[2] M. Salvatores and R. Jacqmin, Uncertainty and target accuracy assessment for innovative systems using recent covariance data evaluations, NEA/WPEC Subgroup 26 Final Report, OECD Nuclear Energy Agency, 2008.

[3] M. Wenner, A. Haghighat, J. Adams, A. Carlson, S. Grimes, and T. Massey, Nucl. Sci. Eng. **170**, 207 (2012).

[4] OECD Nuclear Energy Agency, Nuclear Data High-Priority Request List, available at http://www.oecd-nea.org/dbdata/hprl/.

[5] International Nuclear Data Evaluation Network, CIELO follow-up: Technical Meeting on Long-term International Collaboration to Improve Nuclear Data Evaluation and Evaluated Data Files, https://www-nds.iaea.org/index-meeting-crp/TM_IAEACIELO/ (2017).

[6] N. Otuka, E. Dupont, V. Semkova, B. Pritychenko, A. I. Blokhin, M. Aikawa, S. Babykina, M. Bossant, G. Chen, S. Dunaeva, R. A. Forrest, T. Fukahori, N. Furutachi, S. Ganesan, Z. Ge, O. O. Gritzay, M. Herman, S. Hlavač, K. Katō, B. Lalremruata, Y. O. Lee, A. Makinaga, K. Matsumoto, M. Mikhaylyukova, G. Pikulina, V. G. Pronyaev, A. Saxena, O. Schwerer, S. P. Simakov, N. Soppera, R. Suzuki, S. Takács, X. Tao, S. Taova, F. Tárkányi, V. V. Varlamov, J. Wang, S. C. Yang, V. Zerkin, and Y. Zhuang, Nucl. Data Sheets **120**, 272 (2014).

[7] A. Koning and J. Delaroche, Nucl. Phys. A **713**, 231 (2003).

[8] R. Beyer, A. R. Junghans, P. Schillebeeckx, I. Sirakov, T.-Y. Song, D. Bemmerer, R. Capote, A. Ferrari, A. Hartmann, R. Hannaske, J. Heyse, H. I. Kim, J. W. Kim, T. Kögler, C. W. Lee, Y.-O. Lee, R. Massarczyk, S. E. Müller, T. P. Reinhardt, M. Röder, K. Schmidt, R. Schwengner, T. Szücs, M. P. Takács,

A. Wagner, L. Wagner, and S.-C. Yang, Eur. Phys. J. A **54**, 81 (2018).

[9] R. L. Becker, W. G. Guindon, and G. J. Smith, Nucl. Phys. **89**, 154 (1966).

[10] A. Begum, Nucl. Sci. Appl., Ser. B **12/13**, 13 (1981).

[11] J. R. Beyster, M. Walt, and E. W. Salmi, Phys. Rev. **104**, 1319 (1956).

[12] N. A. Bostrom, I. L. Morgan, J. T. Prud'homme, P. L. Okhuysen, and O. M. Hudson, Jr., Interaction of fast neutrons in iron, lead, oxygen and hydrogen, Wright Air Development Center Reports 59-31, 1959.

[13] S. W. Cierjacks and I. Schouky, in *Proceedings of an International Conference on Neutron Physics and Nuclear Data for Reactors and Other Applied Purposes* (OECD Nuclear Energy Agency, Paris, 1978), p. 187.

[14] L. Cranberg and J. S. Levin, Phys. Rev. **103**, 343 (1956).

[15] R. B. Galloway and A. Waheed, Nucl. Phys. A **318**, 173 (1979).

[16] W. B. Gilboy and J. H. Towle, Nucl. Phys. **64**, 130 (1965).

[17] R. W. Hill, Bull. Am. Phys. Soc. **1**, 174(F1) (1956).

[18] R. W. Hill, Phys. Rev. **109**, 2105 (1958).

[19] B. Holmqvist, T. W. S. G. Johansson, G. Lodin, A. Kiss, B. Gustavsson, and B. Antolkovic, Neutron Elastic Scattering Cross Sections, Experimental Data and Optical Model Cross Section Calculations, Aktiebolaget Atomenergi, Stockholm/Studsvik Report AE-366, 1969.

[20] B. Holmqvist, S. G. Johansson, G. Lodin, M. Salama, and T. Wiedling, A Neutron Elastic Scattering Study of Chromium, Iron and Nickel in the Energy Region 1.77 to 2.76 MeV, Aktiebolaget Atomenergi, Stockholm/Studsvik Report AE-385, 1970.

[21] B. Holmqvist and T. Wiedling, Optical model analyses of experimental fast neutron elastic scattering data, Aktiebolaget Atomenergi, Stockholm/Studsvik Report AE-430, 1971.

[22] J. C. Hopkins and M. G. Silbert, Nucl. Sci. Eng. **19**, 431 (1964).

[23] A. Jacquot and C. Rousseau, Nucl. Phys. **84**, 239 (1966).

[24] W. E. Kinney and F. G. Perey, Neutron elastic- and inelastic-scattering cross sections for ^{56}Fe in the energy range 4.19 to 8.56 MeV, Oak Ridge National Laboratory Report ORNL-4515, 1970.

[25] W. E. Kinney and J. W. McConnell, in *International Conference on Interactions of Neutrons with Nuclei, Lowell, Massachusetts*, edited by E. Sheldon (Energy Research and Development Administration, Technical Information Center, Springfield, VA, 1976), p. 1319.

[26] I. A. Korzh, V. A. Mishchenko, E. N. Mozhzhukhin, N. M. Pravdivij, and I. E. Sanzhur, Ukr. Fiz. Zh. **22**, 87 (1977).

[27] H. H. Landon, A. J. Elwyn, G. N. Glasoe, and S. Oleksa, Phys. Rev. **112**, 1192 (1958).

[28] M. K. Machwe, D. W. Kent, Jr., and S. C. Snowdon, Phys. Rev. **114**, 1563 (1959).

[29] M. V. Pasechnik, I. F. Barchuk, I. A. Totskiy, V. I. Strizhak, A. M. Korolev, Y. V. Gofman, G. N. Lovchikova, E. A. Koltypin, and G. B. Yankov, in *Second International Atomic Energy Conference*, Vol. 15 (United Nations, Geneva, 1958), p. 18.

[30] M. J. Poole, Philos. Mag. **44**, 1398 (1953).

[31] V. I. Popov, At. Energiya **3**, 498 (1957).

[32] O. A. Salnikov, At. Energiya **3**, 106 (1957).

[33] A. Smith and P. Guenther, Nucl. Sci. Eng. **73**, 186 (1980).

[34] A. B. Smith, Nucl. Phys. A **605**, 269 (1996).

[35] Y. Tomita, K. Tsukada, M. Maruyama, and S. Tanaka, in *Nuclear Data for Reactors Conference Proceedings*, Vol. 2,

Helsinki (International Atomic Energy Agency, Vienna, 1970), pp. 301–304.

[36] K. Tsukada, S. Tanaka, and M. Maruyama, J. Phys. Soc. Jpn. **16**, 166 (1961).

[37] K. Tsukada, S. Tanaka, Y. Tomita, and M. Maruyama, Nucl. Phys. A **125**, 641 (1969).

[38] M. Walt and J. R. Beyster, Phys. Rev. **98**, 677 (1955).

[39] E. Almen-Ramstrom, A systematic study of neutron inelastic scattering in the energy range 2.0 to 4.5 MeV, Aktiebolaget Atomenergi, Stockholm/Studsvik Report AE-503, 1975.

[40] A. W. Barrows, R. C. Lamb, D. Velkley, and M. T. McEllistrem, Nucl. Phys. A **107**, 153 (1968).

[41] R. Beyer, R. Schwengner, R. Hannaske, A. R. Junghans, R. Massarczyk, M. Anders, D. Bemmerer, A. Ferrari, A. Hartmann, T. Kögler, M. Röder, K. Schmidt, and A. Wagner, Nucl. Phys. A **927**, 41 (2014).

[42] P. Boschung, J. T. Lindow, and E. F. Shrader, Nucl. Phys. A **161**, 593 (1971).

[43] J. G. Degtjarev and V. N. Protopopov, At. Energiya **23**, 568 (1967).

[44] S. F. Hicks, J. R. Vanhoy, A. J. French, S. L. Henderson, T. J. Howard, R. L. Pecha, Z. C. Santonil, B. P. Crider, S. Liu, M. T. Mcellistrem, E. E. Peters, F. M. Prados-Estevez, T. J. Ross, and S. W. Yates, EPJ Web Conf. **93**, 02002 (2015).

[45] W. E. Kinney, Neutron elastic and inelastic scattering from ^{56}Fe from 4.60 to 7.55 MeV, Oak Ridge National Lab. Technical Memo ORNL-TM-2052, 1968.

[46] L. S. Lebedev, J. A. Nemilov, A. V. Orlovskij, and L. A. Pobedonostsev, Yadernye Konstanty **24**, 3 (1977).

[47] A. Negret, C. Borcea, and A. J. M. Plompen, Phys. Rev. C **88**, 027601 (2013).

[48] Y. A. Nemilov, L. A. Pobedonostsev, and E. L. Teterin, At. Energiya **53**, 194 (1982).

[49] W. L. Rodgers, E. F. Shrader, and J. T. Lindow, Neutron scattering from C12, Fe54, Fe56, Cu65, Ni58, and Ni60., Chicago Operations Office, A.E.C., Contract report COO-1573-33, 1967.

[50] M. Salama, Atomkernenergie **37**, 221 (1981).

[51] T. Schweitzer, D. Seeliger, and K. Seidel, Kernenergie **20**, 174 (1977).

[52] E. Pirovano, Neutron scattering cross section measurements with a new scintillator array, Ph.D. thesis, Ghent University, 2017, IAEA INDC report INDC(BLG)-2.

[53] J. Meija, T. Coplen, M. Berglund, W. Brand, P. D. Bièvre, M. Gröning, N. Holden, J. Irrgeher, R. Loss, T. Walczyk, and T. Prohaska, Pure Appl. Chem. **88**, 265 (2016).

[54] J. Meija, T. Coplen, M. Berglund, W. Brand, P. D. Bièvre, M. Gröning, N. Holden, J. Irrgeher, R. Loss, T. Walczyk, and T. Prohaska, Pure Appl. Chem. **88**, 293 (2016).

[55] H. Junde, H. Su, and Y. Dong, Nucl. Data Sheets **112**, 1513 (2011).

[56] Y. Dong and H. Junde, Nucl. Data Sheets **121**, 1 (2014).

[57] M. Bhat, Nucl. Data Sheets **85**, 415 (1998).

[58] C. D. Nesaraja, S. D. Geraedts, and B. Singh, Nucl. Data Sheets **111**, 897 (2010).

[59] D. Brown, M. Chadwick, R. Capote, A. Kahler, A. Trkov, M. Herman, A. Sonzogni, Y. Danon, A. Carlson, M. Dunn, D. Smith, G. Hale, G. Arbanas, R. Arcilla, C. Bates, B. Beck, B. Becker, F. Brown, R. Casperson, J. Conlin *et al.*, Nucl. Data Sheets **148**, 1 (2018), Special Issue on Nuclear Reaction Data.

[60] OECD Nuclear Energy Agency, JEFF-3.3 Evaluated Data Library, available at https://www.oecd-nea.org/dbdata/jeff/jeff33/index.html (2017).

[61] K. Shibata, O. Iwamoto, T. Nakagawa, N. Iwamoto, A. Ichihara, S. Kunieda, S. Chiba, K. Furutaka, N. Otuka, T. Ohsawa, T. Murata, H. Matsunobu, A. Zukeran, S. Kamada, and J. I. Katakura, J. Nucl. Sci. Technol. **48**, 1 (2011).

[62] H. Klein and S. Neumann, in International Workshop on Neutron Field Spectrometry in Science, Technology and Radiation Protection [Nucl. Instrum. Methods Phys. Res., Sect. A **476**, 132 (2002)].

[63] H. Klein, Radiat. Prot. Dosim. **107**, 95 (2003).

[64] N. Kornilov, I. Fabry, S. Oberstedt, and F.-J. Hambsch, Nucl. Instrum. Methods Phys. Res., Sect. A **599**, 226 (2009).

[65] A. Tomanin, J. Paepen, P. Schillebeeckx, R. Wynants, R. Nolte, and A. Lavietes, Nucl. Instrum. Methods Phys. Res., Sect. A **756**, 45 (2014).

[66] X-5 Monte Carlo Team, MCNP - A General Monte Carlo N-Particle Transport Code, Version 5, Los Alamos National Laboratory Report No. LA-UR-03-1987, 2003.

[67] W. Mondelaers and P. Schillebeeckx, Notiziario Neutroni e Luce di Sincrotrone **11**, 19 (2006).

[68] D. Ene, C. Borcea, S. Kopecky, W. Mondelaers, A. Negret, and A. Plompen, Nucl. Instrum. Methods Phys. Res., Sect. A **618**, 54 (2010).

[69] R. Beyer, E. Birgersson, Z. Elekes, A. Ferrari, E. Grosse, R. Hannaske, A. Junghans, T. Kögler, R. Massarczyk, A. Matić, R. Nolte, R. Schwengner, and A. Wagner, Nucl. Instrum. Methods Phys. Res., Sect. A **723**, 151 (2013).

[70] Eljen Technology, EJ301, EJ309 data sheet, available at http://www.eljentechnology.com/products/liquid-scintillators/ej-301-ej-309.

[71] Eljen Technology, EJ315 data sheet, available at http://www.eljentechnology.com/products/liquid-scintillators/ej-315.

[72] D. Gedcke and W. McDonald, Nucl. Instrum. Methods **55**, 377 (1967).

[73] V. Modamio, J. Valiente-Dobón, G. Jaworski, T. Hüyük, A. Triossi, J. Egea, A. D. Nitto, P.-A. Söderström, J. A. Ros, G. de Angelis, G. de France, M. Erduran, S. Ertürk, A. Gadea, V. González, J. Kownacki, M. Moszynski, J. Nyberg, M. Palacz, E. Sanchis, and R. Wadsworth, Nucl. Instrum. Methods Phys. Res., Sect. A **775**, 71 (2015).

[74] F. Brooks, Nucl. Instrum. Methods **4**, 151 (1959).

[75] C. Rouki, P. Archier, C. Borcea, C. D. S. Jean, J. Drohé, S. Kopecky, A. Moens, N. Nankov, A. Negret, G. Noguère, A. Plompen, and M. Stanoiu, Nucl. Instrum. Methods Phys. Res., Sect. A **672**, 82 (2012).

[76] K. Gamage, M. Joyce, and N. Hawkes, Nucl. Instrum. Methods Phys. Res., Sect. A **642**, 78 (2011).

[77] J. Polack, M. Flaska, A. Enqvist, C. Sosa, C. Lawrence, and S. Pozzi, Nucl. Instrum. Methods Phys. Res., Sect. A **795**, 253 (2015).

[78] L. W. Townsend, Neutron-deuterium cross section evaluation, Final Technical Report, AECL Purchase Order 217739, Atomic Energy of Canada Limited, 2006.

[79] E. Pirovano, R. Beyer, A. R. Junghans, N. Nankov, R. Nolte, M. Nyman, and A. J. M. Plompen, Phys. Rev. C **95**, 024601 (2017).

[80] A. Carlson, Metrologia **48**, S328 (2011).

[81] M. Herman, A. Trkov, R. Capote, G. Nobre, D. Brown, R. Arcilla, Y. Danon, A. Plompen, S. Mughabghab, Q. Jing, G. Zhigang, L. Tingjin, L. Hanlin, R. Xichao, L. Leal, B. Carlson, T. Kawano, M. Sin, S. Simakov, and K. Guber, Nucl. Data Sheets **148**, 214 (2018), Special Issue on Nuclear Reaction Data.